Pergamon

Geochimica et Cosmochimica Acta, Vol. 64, No. 16, pp. 2879–2894, 2000

0016-7037/00 $20.00 + .00

PII S0016-7037(00)00396-3

Major element chemical and isotopic compositions of refractory inclusions in C3 chondrites: The separate roles of condensation and evaporation

LAWRENCE GROSSMAN,† DENTON S. EBEL, STEVEN B. SIMON,* ANDREW M. DAVIS,† FRANK M. RICHTER, and NIGEL M. PARSAD
Department of the Geophysical Sciences, The University of Chicago, 5734 South Ellis Ave., Chicago, IL 60637, USA

(*Received December* 20, 1999; *received in revised form February* 28, 2000; *accepted March* 7, 2000)

Abstract—Literature data for major element oxide compositions of most coarse-grained Types A and B inclusions in CV3 chondrites may be in error due to non-representative sampling of spinel relative to other phases because of small sample sizes. When reported compositions are corrected to the solar CaO/Al_2O_3 ratio by addition or subtraction of spinel, distinct trends result on oxide–oxide plots. These trends lie close to trajectories of bulk compositions of equilibrium condensates calculated for solar or dust-enriched gases under various conditions, except on a plot of MgO vs. SiO_2 contents, where there is considerable scatter of the data points to the MgO-poor side of the condensation trajectory. The irreversible process of evaporative mass loss from a liquid droplet into an unsaturated H_2 gas is modeled as a series of small equilibrium steps. This model is used to show that evolutionary paths of CMAS liquid compositions are identical for evaporation at all P_{H_2} from 1×10^{-15} to 1 bar, with the ratio of the fraction of the SiO_2 evaporated to that for MgO increasing both with increasing temperature from 1700 to 2000 K and with increasing SiO_2 content of the starting composition. Such calculations show that compositions of most Type B inclusions can be explained by non-equilibrium evaporation of 10 to 30% of the MgO and 0 to 15% of the SiO_2 into an H_2 gas at 1700 K from liquid droplets whose compositions originated on any one of many possible equilibrium condensation trajectories. Some Type As may have suffered similar evaporative losses of MgO and SiO_2 but at higher temperature. This degree of evaporation is consistent with the amount of Mg and Si isotopic mass fractionation observed in Types A and B inclusions. Evaporation probably happened after most Mg and Si were removed from the nebular gas into lower-temperature condensates. *Copyright © 2000 Elsevier Science Ltd*

1. INTRODUCTION

In Allende and other CV3 chondrites, there are two varieties of coarse-grained, refractory inclusions distinguished by their mineralogical compositions. Type A contain melilite, spinel, very minor perovskite and rare hibonite; and Type B are composed of melilite, spinel, major amounts of fassaitic clinopyroxene, and relatively minor anorthite. Because these mineral assemblages are the same as those predicted to be in very high-temperature equilibrium with gases of various cosmic compositions, some workers (e.g., Grossman, 1972) consider them to be the earliest condensates from the solar nebula, while others (e.g., Chou et al., 1976) believe them to be the last residues of evaporation of chondritic matter. Because these two processes are thermodynamically equivalent, it has been assumed correctly that the resulting chemical and mineralogical compositions are indistinguishable from one another. In this paper, re-evaluation of existing data on major element compositions of refractory inclusions allows an assessment of the degree of departure of their compositions from those expected from equilibrium condensation or evaporation. In addition, new calculations are presented which predict that the evolution of chemical compositions of non-ideal $CaO–MgO–Al_2O_3–SiO_2$ (abbreviated as CMAS) liquids undergoing non-equilibrium evaporation into vacuum and into pure H_2 gas is not the same as predicted for equilibrium condensation from or evaporation into a gas of solar composition. This evaporation model is used to explain simultaneously the departure of major element compositions of refractory inclusions from the equilibrium condensation trajectory and the degree of mass fractionation of Mg and Si isotopic compositions observed in such inclusions by Molini–Velsko et al. (1986) and Clayton et al. (1988).

* Author to whom correspondence should be addressed (sbs8@midway.uchicago.edu).
† Also at Enrico Fermi Institute, The University of Chicago, Chicago, IL, USA.

2. MAJOR ELEMENT COMPOSITIONS

2.1. Sampling and Analysis Techniques

Refractory inclusions in Allende and other members of the oxidized subgroup of CV3 chondrites underwent extensive, relatively low-temperature secondary alteration, a process which introduced volatile elements and may have also preferentially removed some refractory elements relative to others. Type As seem to be more affected than Type Bs (MacPherson et al., 1988). In this section, therefore, only those refractory inclusions are used whose major element compositions were obtained by techniques designed to avoid or correct for effects of secondary alteration. Beckett (1986) used modal recombination, in which the relative areas of primary phases in each thin section were determined by optical point-counting. These data were assumed to equal the relative volumes of the phases in three dimensions and were combined with densities and average mineral compositions calculated from electron microprobe spot analyses to yield the bulk chemical composition in weight percent of oxides. Nazarov et al. (1982) analyzed one inclusion by modal recombination and three others by defocussed beam analysis, a technique in which an electron microprobe beam is spread out over relatively wide, unaltered regions of polished thin sections of inclusions. Wark (1981) analyzed altered inclusions by rastering polished thin sections under the defocussed beam of an electron microprobe and correcting the analyses for secondary alteration by using abundances of volatile elements and assumptions about identities of the alteration products and compositions of the altered phases. All techniques based on analyses of thin sections run the risk of suffering from non-representative sampling because they are applied to

a very small fraction of the total available material, a 30 μm slice through a spheroidal object whose diameter may be 1 cm or more. Furthermore, the plane of the thin section, far from being deliberately selected, is merely the plane of the saw cut which first revealed the inclusion during slicing of the meteorite.

In contrast to those in Allende, refractory inclusions in Vigarano and other members of the reduced subgroup of CV3 chondrites are very little altered, and it can be safely assumed that bulk chemical analyses are affected insignificantly by secondary alteration. Almost all of the data on these types of inclusions were obtained by instrumental neutron activation analysis (INAA) of samples dug from them but, in most cases, sampling was not optimized for major element analysis. Sampling was often restricted to inclusion interiors to avoid contamination by the surrounding meteorite matrix. Samples taken for INAA were often what remained of larger amounts made into polished thin sections and/or reserved for isotopic studies. As a result, the analyzed samples are seldom more than one mg, are only very small fractions of their host inclusions and are small even compared to the mass of a single melilite or pyroxene crystal within them. There is thus good reason to consider these analyses non-representative.

Inclusions selected for this work are all coarse-grained Types A and B inclusions that are not hibonite-rich from the work of Palme and Wlotzka (1979), Wark (1981), Nazarov et al. (1982), Beckett (1986), and Mao et al. (1990), as well as all those from the reduced subgroup studied by Wark and Lovering (1982), Sylvester et al. (1992), except for 1623-8, and Sylvester et al. (1993), except for one which contains abundant alteration products. The bulk chemical composition of 1623-8 obtained by INAA is quite different from that obtained by modal recombination, as discussed by Sylvester et al. (1992). Because the INAA data come from a single, 749 μg chip removed from 1623-8 rather than from material scraped from a wide area of it, the composition obtained by modal recombination of a several mm^2 area of a thin section is thought to be more representative. All compositions are listed in Table 1, together with the sample number, host meteorite, inclusion type, analytical technique, literature source of the data, and, for those analyzed by INAA, the sample weight. Silica was determined by difference for all samples analyzed by INAA, except for the one studied by Palme and Wlotzka (1979). All analyses were re-normalized to 100 wt.% CaO + MgO + Al_2O_3 + SiO_2, thus removing 0.5 to 1.5 wt.% TiO_2 and all volatile elements from further consideration.

3. COMPARISON WITH CONDENSATION CALCULATIONS

The data from Table 1 are plotted on all six possible oxide–oxide covariation diagrams in Figures 1a–f. The same data were resolved into Spinel–Gehlenite–Forsterite–Anorthite coordinates by the method of Stolper (1982). These data are projected from Spinel onto the Gehlenite–Forsterite–Anorthite plane in Figure 1g, and the Spinel coordinate is plotted against the Anorthite coordinate in Figure 1h. Each diagram also shows three trajectories of bulk chemical composition of the total condensate assemblage, calculated on a TiO_2- and metallic nickel–iron-free basis, for the temperature interval where the composition of the condensate comes closest to those of refractory inclusions. The three trajectories were calculated by using the computer program of Ebel and Grossman (2000), but at conditions selected to illustrate a wide range of condensation paths: a gas of solar composition at a P^{tot} of 10^{-5} bar, where condensation takes place entirely to crystalline phases; a solar gas at a P^{tot} of 10^{-1} bar, where condensation of partially molten CaO-, Al_2O_3-rich assemblages occurs; and at a P^{tot} of 10^{-3} bar in a system enriched in C1 dust relative to gas by a factor of 20 compared to solar composition, where CMAS partial melts also condense (Yoneda and Grossman, 1995).

Inspection of these figures reveals that, despite differences in their condensate phase assemblages, the three composition trajectories lie very close to one another. More importantly, however, the data for refractory inclusions scatter widely about the condensation paths on most diagrams. The close adherence of inclusion compositions to the condensation trajectories in Figure 1d is exceptional. It is clear from the other figures, however, that bulk chemical compositions of refractory inclusions are only generally similar to those predicted for high-temperature condensates, with many inclusions lying very far from the predicted trends. Particularly egregious is the deviation of the data from the condensation paths on the CaO–Al_2O_3 plot, Figure 1a. Because all inclusions selected for this work are hibonite-poor, it can be assumed that they represent high-temperature condensate assemblages that formed below the temperature at which the last hibonite is predicted to react with the gas to form spinel along many condensation paths. This occurs at a temperature below that where both Al and Ca are totally condensed (Yoneda and Grossman, 1995), corresponding to the maximum CaO value on the trajectories on Figure 1a. Below this temperature, condensation of MgO and SiO_2 dilutes both the Al_2O_3 and CaO contents. The expectation from condensation calculations, then, is that all hibonite-poor refractory inclusions should have the solar CaO/Al_2O_3 ratio, and lie along the left arm of the condensation trajectories shown on Figure 1a. Not only do very few of the inclusions lie along that line but they actually form a trend which cross-cuts it, exhibiting a huge range of CaO/Al_2O_3 ratios from 34% below the chondritic value to over 100% above it. Another phenomenon that is very difficult to understand is the distribution of data on the MgO–Al_2O_3 plot, Figure 1b. Not only do the data scatter particularly widely about the condensation paths but also the positions of Type A inclusions relative to Type Bs are enigmatic. Many Type Bs have much higher MgO contents than many Type As with the same Al_2O_3 contents. Because fassaite is predicted to form during condensation by reaction of gaseous Mg and Si with melilite, Type Bs, which are fassaite-rich, are expected to have higher MgO contents than Type As, which are melilite-rich and contain very little fassaite. Although this is what is observed, the massive addition of MgO and SiO_2 to make fassaite must also dilute the Al_2O_3 contents, and this is not observed.

Agreement between compositions of refractory inclusions and those predicted from condensation calculations is much better on some of these plots than on others. The data plot very tightly along the predicted SiO_2–Al_2O_3 trend, Figure 1d, for example, although it is unclear why the range of SiO_2 contents is the same in As and Bs, considering the large amount of SiO_2 that must be added to Type A assemblages to yield Type Bs. Also, one of the three calculated condensate trajectories trends right through the analytical data on the Stolper projection, Figure 1g, although, when viewed in the direction orthogonal to that projection, Figure 1h, the data scatter enormously about the calculated trajectories.

4. NON-REPRESENTATIVE SAMPLING

Also plotted on this set of eight diagrams are compositions of the pure phases that constitute the inclusions, spinel ($MgAl_2O_4$) and anorthite ($CaAl_2Si_2O_8$), as well as compositions of the end-member components of the solid solution phases in the inclusions, gehlenite ($Ca_2Al_2SiO_7$) and åkermanite ($Ca_2MgSi_2O_7$) in melilite; and diopside ($CaMgSi_2O_6$), calcium–Tschermak's mol-

Table 1. Petrographic types, bulk compositions, and literature sources of coarse-grained refractory inclusions.

Sample no.	Meteorite	Inclusion type[a]	Analytic method[b]	CaO	MgO	Al_2O_3	SiO_2	Reference
20A, B	Allende	A	DBA	38.48	3.64	35.25	22.63	1
20A, J	Allende	A	DBA	38.30	3.55	36.07	22.09	1
20B, L	Allende	A	DBA	38.93	2.92	35.51	22.64	1
3529, 33	Allende	A	DBA	38.03	4.35	36.68	20.93	1
A70	Allende	A	DBA	28.59	9.56	46.39	15.46	1
4691	Allende	A	DBA	34.66	6.24	39.57	19.53	1
TS-2	Allende	CTA	Modal recomb.	34.19	10.36	29.18	26.27	2
TS-12	Allende	CTA	Modal recomb.	35.67	6.01	36.06	22.26	2
TS-19	Allende	CTA	Modal recomb.	37.15	6.47	31.19	25.19	2
TS-32	Allende	CTA	Modal recomb.	39.92	5.76	26.01	28.31	2
TS-24	Allende	FTA	Modal recomb.	35.48	5.82	37.07	21.62	2
TS-25	Allende	CTA	Modal recomb.	36.36	4.40	36.95	22.29	2
TS-27	Allende	CTA	Modal recomb.	35.88	3.91	40.88	19.34	2
TS-29	Allende	FTA	Modal recomb.	39.90	2.50	33.77	23.83	2
3536-2	Leoville	CTA	INAA (13.9 μg)	38.75	5.52	23.62	32.11	3
L1	Leoville	CTA	INAA (1.158 mg)	40.23	5.12	36.64	18.01	4
L4	Leoville	FTA	INAA (482.1 μg)	35.09	7.96	35.60	21.34	4
477-5	Vigarano	CTA	INAA (49.5 μg)	39.06	2.87	36.60	21.47	5
Ef1	Efremovka	CTA	INAA (570.5 μg)	38.21	4.17	35.68	21.93	4
Ef2	Efremovka	CTA	INAA (224.0 μg)	41.69	4.70	30.18	23.42	4
Ef3	Efremovka	CTA	INAA (1.108 mg)	31.86	8.99	36.01	23.14	4
E2	Efremovka	CTA	Modal recomb.	33.52	8.05	37.81	20.61	6
TS-23	Allende	B1	Modal recomb.	33.30	8.70	28.72	29.28	2
TS-33	Allende	B1	Modal recomb.	30.54	7.85	33.74	27.86	2
TS-34	Allende	B1	Modal recomb.	33.26	8.65	29.15	28.94	2
TS-4	Allende	B2	Modal recomb.	26.65	11.37	31.71	30.27	2
TS-8	Allende	B2	Modal recomb.	20.47	15.16	39.09	25.29	2
TS-20	Allende	B2	Modal recomb.	30.31	10.66	28.69	30.34	2
TS-21	Allende	B2	Modal recomb.	29.49	10.25	27.89	32.37	2
TS-22	Allende	B2	Modal recomb.	23.22	13.41	39.58	23.79	2
TS-31	Allende	B2	Modal recomb.	27.74	11.31	26.66	34.29	2
LEO 3537-1	Leoville	B2	INAA (652.1 μg)	23.88	13.98	35.61	26.53	3
L2	Leoville	B2	INAA (622.1 μg)	25.59	10.81	33.33	30.28	4
L5	Leoville	B2	INAA (656.9 μg)	33.20	6.98	33.60	26.21	4
Leo 3537-2	Leoville	B1	INAA (1.049 mg)	25.82	14.04	35.76	24.39	5
Leo-1	Leoville	B1	DBA	25.26	10.84	32.11	31.80	7
Leo-1	Leoville	B	INAA (47.9 mg)	19.44	14.61	37.04	28.91	8
VIG.477	Vigarano	B1	DBA	29.61	11.78	33.09	25.51	7
Vig 477-B	Vigarano	B1	INAA (1.163 mg)	23.66	17.36	38.53	20.45	5
Vig 1623-8	Vigarano	B2	Modal recomb.	30.68	7.09	30.75	31.48	9
Vig 1623-11	Vigarano	B2	INAA (96.9 μg)	33.75	8.38	30.78	27.09	5
Vig2	Vigarano	B1	INAA (1.546 mg)	31.73	12.45	25.82	30.00	4
E1	Efremovka	B	DBA	22.18	12.64	35.61	29.57	6
E9	Efremovka	B	DBA	27.32	12.08	23.40	37.21	6

[a] CTA: Compact Type A; FTA: Fluffy Type A. Some inclusions were studied before the CTA-FTA, B1-B2 subtypes were recognized; such inclusions are simply designated "A" or "B", respectively.

[b] DBA: defocussed beam analysis; Modal recomb.: modal recombination—bulk compositions calculated from modal abundances of phases, and their average compositions and densities. INAA: instrumental neutron activation analysis. Sample weights are given in parentheses. Analyses are normalized to 100 wt.% CaO + MgO + Al_2O_3 + SiO_2. References: (1) Wark (1981); (2) Beckett (1986); (3) Mao et al. (1990); (4) Sylvester et al. (1993); (5) Sylvester et al. (1992); (6) Nazarov et al. (1982); (7) Wark and Lovering (1982); (8) Palme and Wlotzka (1979); (9) MacPherson and Davis (1993).

ecule ($CaAl_2SiO_6$), Ti^{3+}-bearing pyroxene ($CaTiAlSiO_6$), and Ti^{4+}-bearing pyroxene ($CaTiAl_2O_6$) in fassaite. For reasons outlined above, it is reasonable to suspect the representativeness of each analysis in Table 1. It is instructive to consider that the sample of each inclusion whose analysis is plotted on these diagrams is a mixture of these eight components that are more or less physically separable from one another, even in the case of the solid solution end-members because of mineralogical zonation. If poor sampling is the reason for the deviation of the composition of an inclusion from the condensation trends, then one or more of these components must have been oversampled relative to the others compared to the bulk inclusion.

Spinel's composition lies on the opposite side of the condensation trends from the compositions of the melilite components in Figures 1a,b,e,f. This suggests that a population of inclusion compositions that originally lay along the condensation trends could have been artificially dispersed about the trends in those figures by sampling non-representative proportions of spinel relative to melilite. Furthermore, because the compositions of spinel and the melilite components lie along or close to extensions of the condensation trends in Figures 1c,d, fractionation of these phases from one another during sampling would not affect the close adherence of the data points to the condensation trends in these figures. Also, the close correspon-

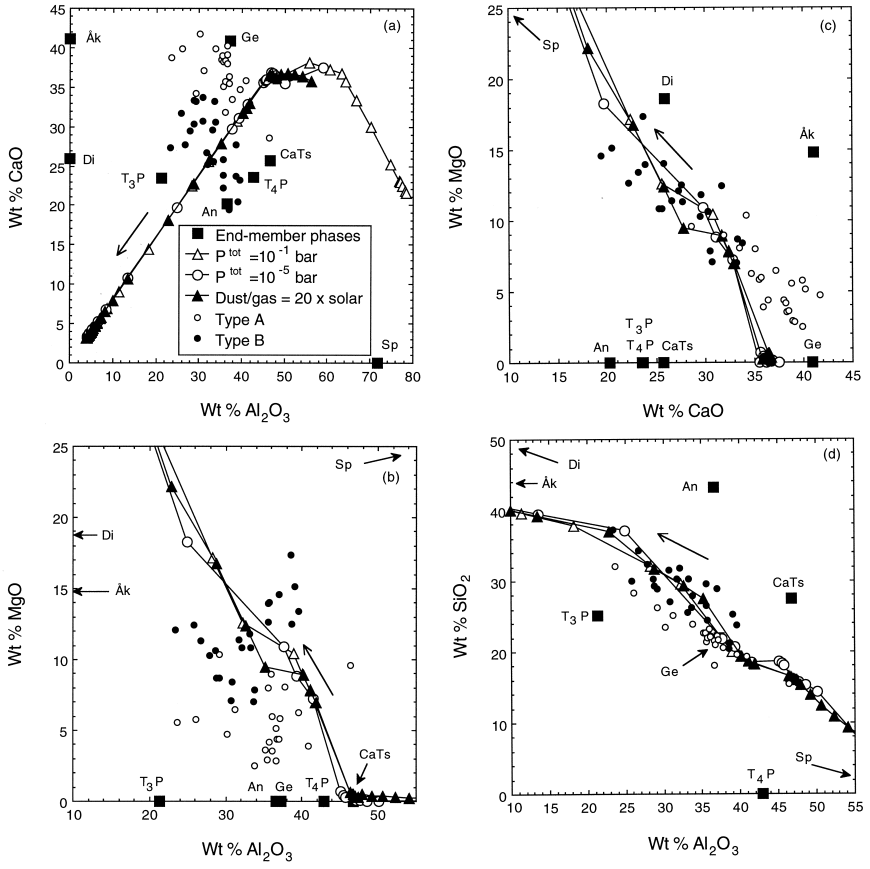

Fig. 1. Raw data for major element oxide concentrations in coarse-grained, Type A (small open circles) and Type B (small closed circles) refractory inclusions, compared to the composition trends of equilibrium condensate assemblages calculated for three sets of conditions, solar composition at $P^{tot} = 1 \times 10^{-1}$ bar (triangles) and 1×10^{-5} bar (large open circles); and a composition enriched in C1 dust relative to gas by a factor of 20 relative to solar composition, at 1×10^{-3} bar (large filled triangles). Symbols along condensate trends are compositions calculated at 10 K intervals. (a) CaO vs. Al_2O_3; (b) MgO vs. Al_2O_3; (c) MgO vs. CaO; (d) SiO_2 vs. Al_2O_3; (e) SiO_2 vs. CaO; (f) SiO_2 vs. MgO; (g) projected from Spinel onto the Anorthite–Gehlenite–Forsterite plane, by using the method of Stolper (1982); and (h) Spinel–Anorthite, orthogonal to (g). Where possible, compositions of end-member components are plotted as large filled squares. Unlabelled arrows indicate the direction of decreasing temperature along condensation trends. Sp, spinel; Ge, gehlenite; Åk, åkermanite; Di, diopside; CaTs, calcium–Tschermak's molecule; T_3P, Ti^{3+}-bearing pyroxene component; T_4P, Ti^{4+}-bearing pyroxene component; An, anorthite.

dence between inclusion compositions and the condensation curves in the spinel projection, Figure 1g, would be completely unaffected, as sampling more or less spinel relative to other phases simply moves inclusion compositions up or down in the direction perpendicular to the plane of the figure but leaves the projected positions of the data points in the plane of the figure exactly where they are.

Let us assume that the composition of each Type A and B inclusion is that of the equilibrium condensate assemblage at a specific temperature, and that the only reason measured inclusion compositions deviate from some of the calculated composition trajectories is that the samples taken for analysis contain more or less spinel relative to other phases compared to the actual compositions. To test this hypothesis, a calculation was done in which sufficient Al in the form of $MgAl_2O_4$ was either added to or subtracted from the bulk chemical composition of each inclusion in Table 1 such that the corrected composition has the cosmic CaO/Al_2O_3 ratio, and the results are plotted in Figures 2a–g. A counterpart to Figure 1g is not shown, as it is unchanged when the corrected data are substituted for the raw data. On almost every figure, a dramatic reduction in the scatter of the data points relative to one another occurs, with the broad cluster characteristic of each plot in Figure 1 transformed into a narrow curvilinear trend in its counterpart in Figure 2. Particularly impressive is the tight trend produced on the SiO_2–CaO plot, Figure 2e, as the added spinel contains neither of these oxides. Furthermore, the trends of the corrected inclusion compositions match the condensation trajectories very closely. The notable exception is the SiO_2–MgO plot, Figure 2f, in which the scatter of the corrected data for Type B inclusions relative to one another and their deviation from the condensation trajectories are seen to be only slightly reduced compared to their uncorrected counterparts in Figure 1f.

Evidence that relatively small sample sizes are the reason for non-chondritic CaO/Al_2O_3 ratios in the analyses in Table 1 comes from the work of Clarke et al. (1970), who used wet chemical means to analyze 1.5 g of material from a Type B inclusion, which they termed a "Type a chondrule." They found

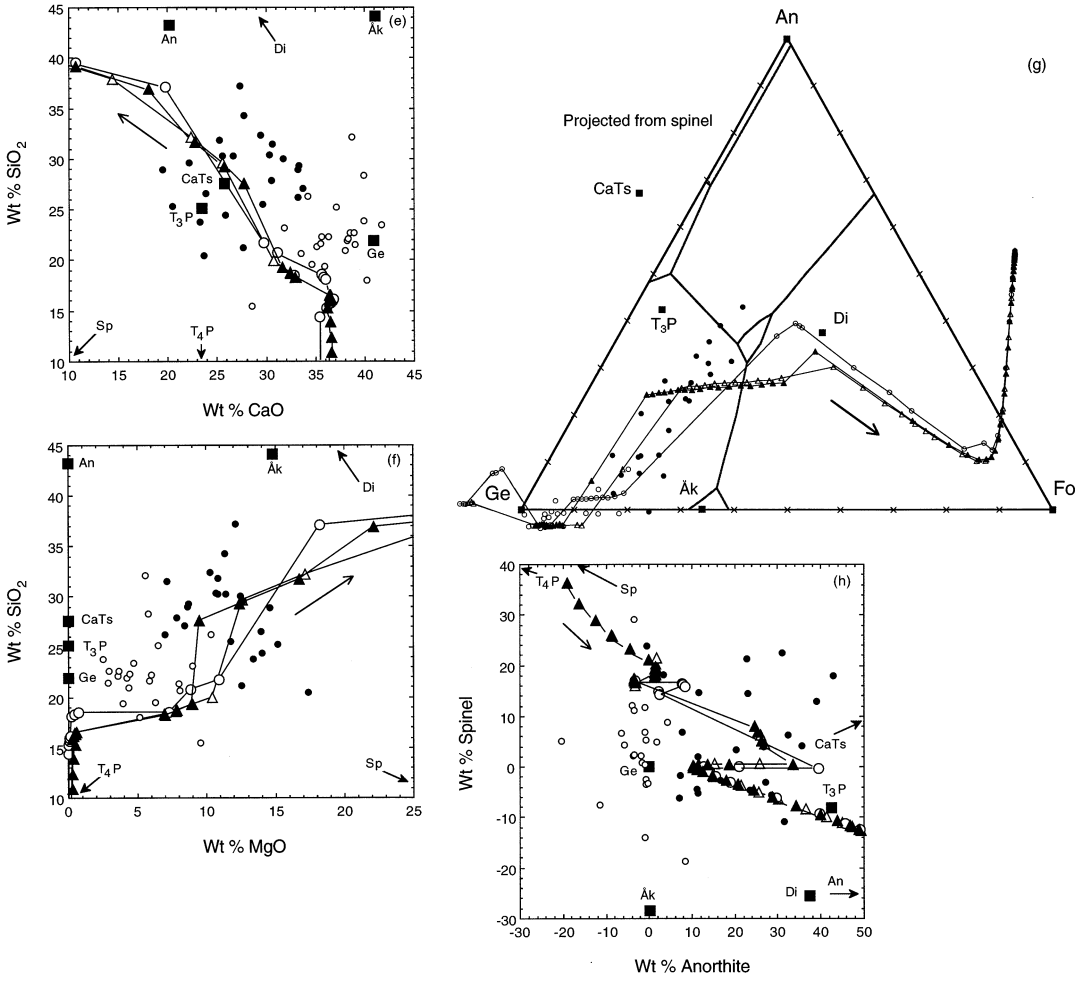

Fig. 1. (Continued)

a CaO/Al_2O_3 ratio only 7% greater than the chondritic value. Similarly, Wänke et al. (1974) separated an entire, 220 mg, spherical inclusion from Allende and found by INAA of a large amount of it that its CaO/Al_2O_3 ratio is 4% less than the chondritic value, a deviation less than their analytical error. Evidence that the corrected analyses are more accurate than the raw data on Table 1 comes from the much-improved consistency between chemical analyses and mineralogical compositions. On Figures 2b and d, for example, almost all Type B inclusions now have lower Al_2O_3 contents to go along with their higher MgO and SiO_2 contents, respectively, than almost all Type As, as is expected for inclusions in which much melilite has been replaced by fassaite.

The assumption that the raw data on Table 1 are inaccurate because of non-representative sampling of spinel relative to other phases can only be justified if spinel is inhomogeneously distributed in these inclusions. Fortunately, abundant petrographic evidence exists for this. Spinel occurs as small (~40 μm), equant crystals poikilitically enclosed in much larger crystals of all silicate phases in the inclusions, but not randomly. Grossman (1975; Fig. 2A) was the first to show that spinel crystals are arranged in long chains with spinel-free areas between the chains in Type A inclusions, and described phenocrysts containing dense concentrations of spinel at one end and virtually no spinel at the other end in Type B inclusions. Wark and Lovering (1977) pointed out that virtually every coarse-grained inclusion has a continuous, ~20 μm thick, outer rim of spinel crystals. Beckett's (1986) modal recombinations overlooked this spinel in every case, as inclusion edges are very heavily altered, and such regions were always avoided. Samples taken for INAA would also have missed this spinel, as inclusion edges were always avoided to reduce matrix contamination. El Goresy et al. (1979) noted that spinel crystals often form dense clusters and spherical shells up to several grains thick around other phases in the interiors of refractory inclusions. Particularly illustrative of the heterogeneous distribution of spinel is a Type A inclusion in Axtell whose only spinel occurs in a dense, nearly monomineralic core (Simon et al., 1999; Fig. 2e). Only very few of the large number of thin sections that could have been made of this inclusion would show this feature; in most, very little spinel would have been seen and its modal amount grossly underestimated.

Figure 3 shows the amount of spinel which had to be added to or subtracted from each inclusion composition separately for each inclusion type and analytical technique. These data suggest that spinel was underestimated in the analysis of almost

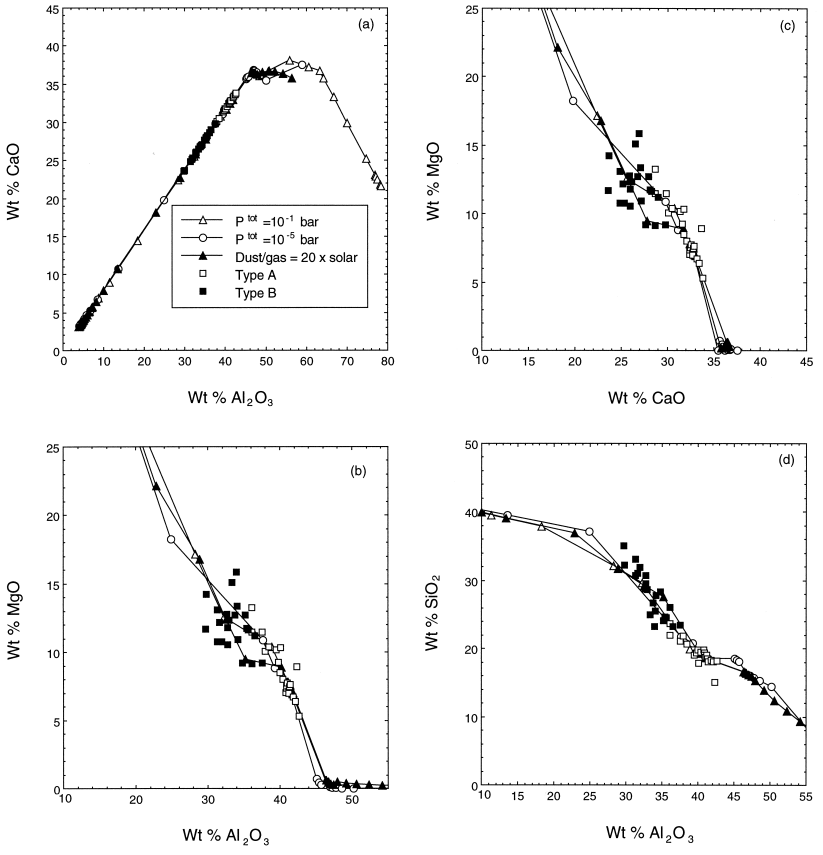

Fig. 2. Major element oxide concentrations in coarse-grained, refractory inclusions, as corrected to the solar CaO/Al_2O_3 ratio by addition or subtraction of stoichiometric $MgAl_2O_4$ to or from the raw data, compared to condensation trajectories. (a) CaO vs. Al_2O_3; (b) MgO vs. Al_2O_3; (c) MgO vs. CaO; (d) SiO_2 vs. Al_2O_3; (e) SiO_2 vs. CaO; (f) SiO_2 vs. MgO; and (g) Spinel vs. Anorthite. Corrected Type A compositions are plotted as small open squares and corrected Type Bs as small filled squares. Otherwise, symbols and abbreviations as in Figure 1.

every Type A inclusion. Perhaps spinel cores like that seen by Simon et al. (1999) are common features of Type A inclusions. In contrast, spinel was undersampled with almost the same frequency as it was oversampled in Type B inclusions, with a slight bias toward undersampling in the thin section-based analyses. For both types of inclusions, the amount of the spinel correction is usually between 10 and 20 wt.%. This amount of added spinel does not lead to unreasonably high spinel contents. In Beckett's (1986) modal recombinations, for example, the precorrection spinel content averages only 9.7 wt.%, the average amount added is 11.2 wt.% and the average corrected spinel content, after re-normalization, is 18.4 wt.%. The largest amount of spinel added to any of the latter samples is 33.9 wt.%, which leads to a spinel content of only 24.3 vol.%.

Assuming that the corrected analytical data in Figure 2 are more accurate than the uncorrected ones, it is now possible to address the questions of which condensation path best fits the data and whether the residual scatter is significant. Unfortunately, although the scatter of the data points is much reduced, it is still comparable to the small differences between condensation paths for different physico-chemical conditions. Of all the plots in Figure 2, those involving MgO show the greatest deviations of the data points, particularly those for Type B inclusions, from possible condensation paths, and this is especially true for the SiO_2–MgO plot, Figure 2f. One interpretation of this is that the inclusions were affected by an additional process after condensation, one that preferentially changed the original MgO and SiO_2 concentrations. These, of course, are the two most volatile oxides considered here, and most prone to evaporation. Had any condensate assemblage whose composition lies on any of the condensation paths in Figure 2 been heated so that it underwent equilibrium evaporation in a gas having the same composition and P^{tot} as the one it had condensed from, however, its composition would have merely evolved along the same composition trend, but in the up-temperature direction. If, on the other hand, a condensate assemblage were heated in a medium different from the one from which it had condensed, in particular, one not saturated in condensable elements, such as a vacuum or a hydrogen gas, the evolution of its composition during evaporation would no longer be restricted to the condensation path.

In an experiment designed to simulate such a process, Davis et al. (1998) reported evaporative loss of Mg and Si relative to Ca and Al when a liquid having the composition of a Type B inclusion was heated in flowing H_2 at 1500°C and $P_{H_2} = 1.8 \times 10^{-4}$ bar. In the next section, we attempt to model this process in an effort to determine in particular the ratio of the amount of Mg lost to the amount of Si lost, and how this ratio varies with

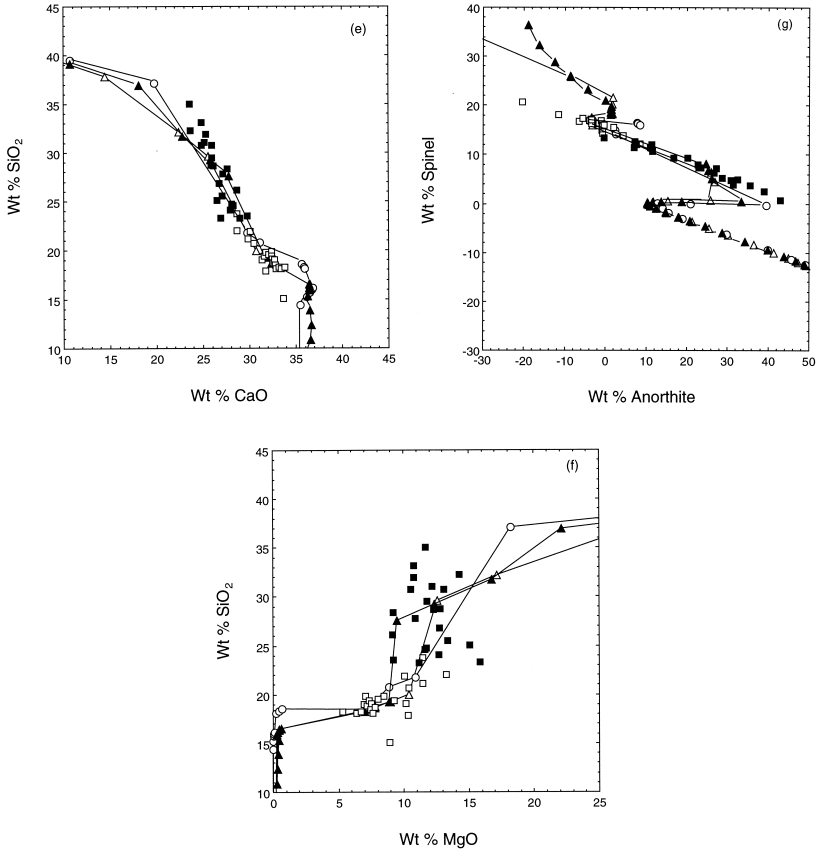

Fig. 2. (Continued)

gas composition, the composition of the starting liquid and temperature.

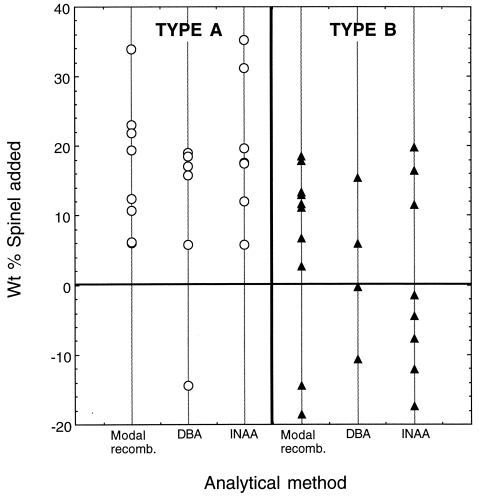

Fig. 3. The amount of the spinel correction applied to each of the inclusions in this study, separately for each inclusion type and analytical method. Modal recombination (Modal recomb.) and defocussed beam analysis (DBA) were performed by electron microprobe analysis of thin sections, while instrumental neutron activation analysis (INAA) was done on bulk samples.

5. EVAPORATION

5.1. Computation of Composition Changes during Evaporation

We imagine a CMAS composition heated at some constant temperature above its liquidus so that it is entirely molten, and that the evaporated material escapes from the surface of the droplet so produced without further interaction with it. To calculate the evolution of the composition of the droplet, this irreversible process is modeled as a series of small, equilibrium evaporation steps. The justification for this approach is discussed below. The problem thus reduces to calculating the vapor pressure over a multicomponent silicate liquid in each of these steps.

In the case of vacuum evaporation, a balanced chemical reaction is written to form every possible gaseous species plus monatomic oxygen from each of the liquid oxide components, e.g., for SiO_2:

$$SiO_{2\,(l)} = SiO_{2(g)} \quad (1)$$

$$SiO_{2\,(l)} = SiO_{(g)} + O_{(g)} \quad (2)$$

and

$$SiO_{2\,(l)} = Si_{(g)} + 2O_{(g)}. \quad (3)$$

For each of these reactions, an equilibrium constant, K_i, is

calculated at the temperature of interest, employing the same thermodynamic database used by Ebel and Grossman (2000) for condensation calculations. The mass-action law for production of each gaseous species of Ca, Mg, Al, and Si is used to express the partial pressure of each species, P_i, explicitly in terms of the activity of its liquid oxide, A. For $Si_{(g)}$, e.g., from Eqn. 3:

$$P_{Si} = K_3 \times A_{SiO_2}/P_O^2. \quad (4)$$

A mass-balance equation is written for only the gaseous species of each element, e.g.,

$$P_{SiO_2} + P_{SiO} + P_{Si} = P_{Si}^{tot}. \quad (5)$$

An expression of the form of Eqn. 4 is substituted for each term in these mass-balance equations. Because the K_i values are known and the activity of each molten oxide can be calculated from the model of Berman (1983) for a CMAS liquid of any composition at the temperature of interest, this results in four equations in five variables. The variables are the partial pressure of monatomic oxygen, P_O; and the total pressure of all species of each of the metallic elements, P_{Ca}^{tot}, P_{Mg}^{tot}, P_{Al}^{tot}, and P_{Si}^{tot}.

A gas-phase reaction between monatomic species is then written for each gaseous species not produced by reactions of the form of Eqns. 1–3. The only one in the present case is:

$$O_{(g)} + O_{(g)} = O_{2(g)}. \quad (6)$$

Calculation of the equilibrium constant for this reaction allows P_{O_2} to be expressed as a function of P_O. This allows a mass-balance equation to be written for oxygen, analogous to Eqn. 5, in which the only new variable is the total pressure of oxygen species, P_O^{tot}. This results in five equations in six variables. The final equation necessary for solving for the partial pressure of each species expresses the condition that evaporated metal atoms cannot leave their oxygen behind in the liquid; i.e., regardless of its gas phase speciation, each metal atom that leaves the liquid must be accompanied in the gas by a number of oxygen atoms in stoichiometric proportion to it in its liquid oxide component. The sixth equation is thus:

$$P_O^{tot} = P_{Ca}^{tot} + P_{Mg}^{tot} + 1.5P_{Al}^{tot} + 2P_{Si}^{tot}. \quad (7)$$

When the sums of terms in each of the five mass-balance equations are substituted for the five terms in Eqn. 7, a single, non-linear equation in one variable, P_O, results, which can be quickly solved by iteration.

The case of evaporation into pure H_2 is very similar. Additional chemical reactions analogous to Eqns. 2 and 3 must be written to form each of the hydrogen-containing gas species by reaction of monatomic $H_{(g)}$ with the liquid oxide components. This introduces P_H in the added expressions analogous to Eqn. 4, additional terms for the H-containing species in the mass-balance equations, and an additional mass-balance equation for hydrogen in which the partial pressures of all H-containing species, multiplied by their stoichiometric coefficients, are summed to equal P_H^{tot}. These include $H_{2(g)}$ and $H_2O_{(g)}$, for which equilibrium constants are calculated through

$$H_{(g)} + H_{(g)} = H_{2(g)} \quad (8)$$

and

$$2H_{(g)} + O_{(g)} = H_2O_{(g)}. \quad (9)$$

The P_{H_2O} term must also be added to the oxygen mass-balance equation. In the calculations presented here, we fix P_{H_2} of the surrounding gas, thereby fixing P_H through Eqn. 8, allow the liquid to react with it, and treat P_H^{tot} as a variable. For evaporation into $H_{2(g)}$ then, Eqn. 7 is solved by iterating on P_O. This allows the partial pressures of all species to be calculated, and P_H^{tot} in the vicinity of the sample is determined from the hydrogen mass-balance equation. All gas species in the system Al–Ca–Mg–Si–O–H considered in the condensation calculations of Yoneda and Grossman (1995) and Ebel and Grossman (2000) were included in the present work.

The partial pressures of all gas species and the total pressure of all species of each element are calculated in each evaporation step. Sufficient gas of this composition is assumed to be removed in each step that one percent of the initial Mg is lost from the droplet. The computed gas composition is used to determine the amount of each of the other elements removed in this step, and the liquid composition is adjusted. For the next evaporation step, the same set of equations must be solved at the same temperature, but the liquid composition, and therefore the activity of each liquid oxide, differs from that in the previous step.

6. RESULTS OF EVAPORATION CALCULATIONS

The calculated gas phase speciation in equilibrium with a liquid having the composition of the equilibrium condensate from a solar gas at 1×10^{-5} bar and 1350 K (35.65 wt.% CaO, 0.70 wt.% MgO, 45.09 wt.% Al_2O_3, and 18.55 wt.% SiO_2) is illustrated in Figures 4a–d as a function of imposed P_{H_2} at 2000 K. This is the gas composition during the first evaporation step. $Mg_{(g)}$ and $SiO_{(g)}$ are the most abundant Mg and Si species and, as expected, their partial pressures are considerably higher than those of the most abundant species of Ca and Al, $Ca_{(g)}$, $AlO_{(g)}$, $AlO_2H_{(g)}$, $AlOH_{(g)}$ and $Al_{(g)}$, over the entire range of P_{H_2}. Because the activities of CaO, MgO, and SiO_2 in the liquid are fixed by the liquid composition and temperature, the partial pressures of CaO, MgO, and SiO_2 do not vary with P_{H_2}. The partial pressures of H-bearing species, including $H_2O_{(g)}$, increase steadily with increasing P_{H_2}. When P_{H_2} reaches $\sim 1 \times 10^{-7}$ bar, P_{H_2O} exceeds P_O and P_{O_2}, and, as P_{H_2} rises above 1×10^{-7} bar, P_{H_2O} increases at the expense of P_O and P_{O_2}. This value of P_{H_2} may be considered the transition P_{H_2}, above which the gas phase chemistry is dominated by $H_{2(g)}$ rather than by the evaporated material. This behavior is very similar to that predicted by Tsuchiyama et al. (1999) in a theoretical treatment of evaporation of forsterite into a simulated solar gas. Below the transition P_{H_2}, the partial pressures of the H-free species remain constant with increasing P_{H_2} at essentially their values calculated for evaporation into a vacuum. Above this P_{H_2}, partial pressures of H-free species, except $O_{(g)}$ and $O_{2(g)}$, and increase with increasing P_{H_2}. This is due to the fact that evaporation now occurs predominantly via reaction of $H_{2(g)}$ with the liquid, forming $H_2O_{(g)}$, rather than $O_{(g)}$, as a product, as in:

$$SiO_{2(l)} + H_{2(g)} = SiO_{(g)} + H_2O_{(g)}. \quad (10)$$

This is a much more favored reaction than its equivalent free

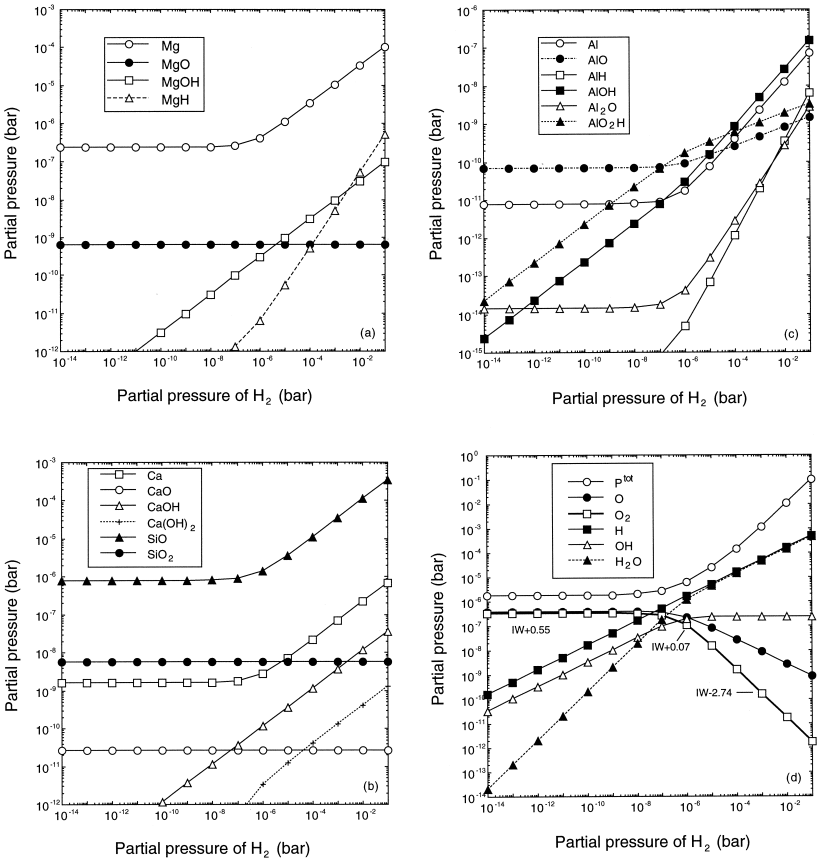

Fig. 4. Composition of the vapor calculated to be in equilibrium with a liquid whose composition is 35.65 wt.% CaO, 0.70% MgO, 45.09% Al_2O_3, and 18.55% SiO_2 at 2000 K, as a function of imposed P_{H_2}. (a) Species of Mg; (b) Species of Ca and Si; (c) Species of Al; and (d) P^{tot} and species of H and O. Logarithms of oxygen fugacities are indicated relative to iron–wüstite (IW) for several points along the curve for O_2.

evaporation reaction Eqn. 2, and this is the reason why partial pressures of all species of Ca, Mg, Al, and Si, and consequently P^{tot}_{Ca}, P^{tot}_{Mg}, P^{tot}_{Al}, and P^{tot}_{Si}, are higher in the H_2-dominated regime than in the droplet-dominated regime. The logarithms of the oxygen fugacity decrease from IW + 0.07 at $P_{H_2} = 1 \times 10^{-6}$ bar to IW − 2.74 at $P_{H_2} = 1 \times 10^{-3}$.

Despite the fact that P^{tot}_{Si} and P^{tot}_{Mg} increase markedly with increasing P_{H_2}, $P^{tot}_{Si}/P^{tot}_{Mg}$ is always ~3.32, varying by only 1% over the entire range of P_{H_2}. This is because the dominant gas species of Si and Mg are always $SiO_{(g)}$ and $Mg_{(g)}$, respectively, making the above ratio approximately equal to P_{SiO}/P_{Mg}. The latter ratio is independent of gas phase speciation, depending only on temperature and the activities of SiO_2 and MgO in the liquid, which are all constant for this calculation. Because $P^{tot}_{Si}/P^{tot}_{Mg}$ is independent of P_{H_2}, the evolution of the liquid composition during evaporation at constant temperature is also independent of P_{H_2}. Because both P^{tot}_{Si} (Fig. 4b) and P^{tot}_{Mg} (Fig. 4a) increase with increasing P_{H_2}, however, greater amounts of material are evaporated at a given temperature with increasing P_{H_2}, accounting for the increasing evaporation rates of CMAS liquids with increasing P_{H_2} at constant temperature seen experimentally by Davis et al. (1998).

An identical calculation for evaporation of the same liquid at 1700 K yields a value of $P^{tot}_{Si}/P^{tot}_{Mg}$ which is again independent of P_{H_2}. The value, 0.635, is much lower than that at 2000 K, however, due to the temperature dependence of the relative equilibrium constants for evaporation of $SiO_{(g)}$ and $Mg_{(g)}$ from the melt. As a consequence of the lower $P^{tot}_{Si}/P^{tot}_{Mg}$, a smaller fraction of the Si is lost from the liquid for a given fraction of the Mg lost at 1700 K than at 2000 K. At 1700 K, the transition from the droplet-dominated regime to the H_2-dominated one is at P_{H_2} ~1×10^{-9} bar, lower than at 2000 K. The oxygen fugacities are also lower at 1700 K, ranging from $\log f_{O_2}$ = IW − 1.94 at $P_{H_2} = 1 \times 10^{-6}$ bar to IW − 4.93 at $P_{H_2} = 1 \times 10^{-3}$.

It is likely that any unsaturated nebular gas into which refractory inclusion precursors evaporated contained other volatile elements which are ignored in this treatment. The most important one is probably carbon. If analogous evaporation calculations were performed with a gas in which CO was assumed to be present in solar proportion to the imposed amount of H, rather than in a pure H_2 gas, the variation of oxygen fugacity with P_{H_2} and the transition P_{H_2} might change, but the relative amount of $SiO_{(g)}$ and $Mg_{(g)}$ evaporated for a given composition and temperature and, thus, the evolution of the liquid composition, would remain unaffected.

As a test of the model, a full evaporation calculation was performed for a sample that was melted and evaporated in 1.8×10^{-4} bar of flowing H_2 at 1773 K by using the experimental facilities and technique described by Hashimoto (1998). The starting composition for both the experiment and the

calculation is 24.61 wt.% CaO, 17.84% MgO, 20.51% Al_2O_3, and 37.04% SiO_2, somewhat more MgO- and SiO_2-rich than a typical Type B inclusion. Under the same P_{H_2} and temperature conditions used in the experiment, the evaporation calculation predicts that the MgO concentration of the residue falls much faster than the SiO_2 concentration, and that CaO and Al_2O_3 contents both increase with increasing degree of evaporation. In Figure 5, the concentrations of the oxides measured in the experimental residue at different degrees of evaporation are compared with the evolution of the concentrations predicted by the evaporation model. Agreement between theory and experiment is excellent up to ~90% of the Mg evaporated, corresponding to ~2.7 wt.% MgO remaining, but, at lower MgO contents, significant discrepancies exist. These are probably related to the fact that melilite precipitated in the three most evaporated experimental residues, causing the composition of the evaporating liquid to be different from the one in our computation.

All other evaporation calculations presented in this paper stop when 50% of the Mg is evaporated. Up to this point, partial pressures of all Ca- and Al-bearing species are so low that Al and Ca are always <0.02% evaporated, regardless of starting composition, temperature and imposed P_{H_2}.

In a full kinetic treatment of evaporation rates of $SiO_{(g)}$ and $Mg_{(g)}$ from a CMAS droplet into a CMAS-free gas, the Hertz–Knudsen equation states:

$$J_{SiO} = \alpha_{SiO} P_{SiO} / (2\pi m_{SiO} kT)^{0.5} \quad (11)$$

and

$$J_{Mg} = \alpha_{Mg} P_{Mg} / (2\pi m_{Mg} kT)^{0.5}, \quad (12)$$

in which k is the Boltzmann constant, T is the absolute temperature, and J, α, P, and m are the flux of atoms from the droplet, the evaporation coefficient, the equilibrium vapor pressure and atomic mass of each evaporating species, respectively. In this kinetic treatment, the evolution of the SiO_2/MgO ratio in the droplet is directly related to the relative loss rates of $SiO_{(g)}$ and $Mg_{(g)}$, obtained by dividing Eqn. 11 by 12:

$$J_{SiO}/J_{Mg} = 0.739(\alpha_{SiO}/\alpha_{Mg})(P_{SiO}/P_{Mg}), \quad (13)$$

where 0.739 is $(m_{Mg}/m_{SiO})^{0.5}$. In the thermodynamic treatment used in this paper, the relative loss rate is taken as P_{SiO}/P_{Mg}, which differs from the rate determined in the kinetic treatment by the factor $0.739(\alpha_{SiO}/\alpha_{Mg})$. In a review of the uncertainty in the value of α for congruent evaporation of forsterite, Tsuchiyama et al. (1999) point out that it varies by a factor of 5 with temperature, gas composition and crystallographic orientation. Little is known about the relative α values of different molecules evaporating from a liquid, but they must be dependent upon temperature and liquid composition. Because of this uncertainty and the fact that measured activities sometimes differ by several tens of percent from those predicted by the Berman (1983) model for CMAS liquids (Chamberlin et al., 1992), we adopted instead the parameterization described above, which is based only on the ratio of the calculated vapor pressures. The justification for doing so is the excellent agreement between model results and experimental observations seen in Figure 5.

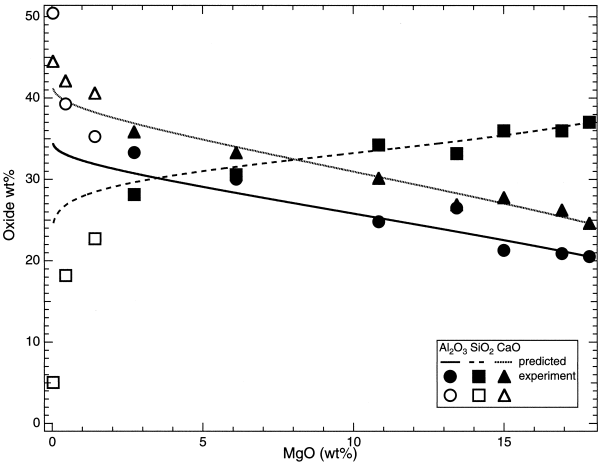

Fig. 5. Comparison of the calculated and experimentally determined evolution of the chemical composition of a liquid during evaporation. The starting composition is 24.61 wt.% CaO, 17.84% MgO, 20.51% Al_2O_3, and 37.04% SiO_2. Open symbols are compositions of experimental residues in which melilite precipitated during evaporation.

7. ISOTOPIC CONSTRAINTS ON EXTENT OF MG AND SI EVAPORATION FROM CAI PRECURSORS

In a study of the Ca isotopic composition of refractory inclusions, Niederer and Papanastassiou (1984) found no enrichment favoring the heavy isotopes in coarse-grained inclusions, suggesting that evaporative loss of Ca from these objects was insignificant. Mg and Si, on the other hand, are both known to be mass fractionated in non-FUN, coarse-grained inclusions, and the correlation between the heavy isotope enrichment of Mg and that for Si in these objects was attributed by Clayton et al. (1988) to partial evaporation of these elements from the inclusions.

In Figure 6, the degree of mass fractionation, F, of Si relative to NBS-28 quartz is plotted against that for Mg relative to Burma spinel for coarse-grained inclusions. The data plotted are for samples 3675A, AL15-5, Egg-1, Egg-2, F2, F3, F6, F7, F11, and F12 taken from the review by Clayton et al. (1988), and for Vigarano inclusions 1623-2 and 1623-8 from Clayton et al. (1987) for Si and Loss et al. (1994) for Mg. For Mg, all samples are enriched in the heavy isotopes but, for Si, one is slightly depleted in the heavy isotopes and all the rest are enriched. While no Mg isotopic variation has been reported among bulk meteorites and terrestrial samples, Molini–Velsko et al. (1986) found that bulk meteorites are depleted in ^{30}Si relative to ^{28}Si compared to NBS-28 by 0.55‰ on average. Because average terrestrial and average lunar Si are similarly depleted, we assume that this value represents the mean Si isotopic composition of the solar system, and that coarse-grained inclusions condensed with an initial F_{Si} of −0.28‰/amu. All of the F_{Si} data from Figure 6 were thus adjusted upward by 0.28‰. After adjustment, one inclusion, F6, a heavily altered Type A, still has a negative F_{Si}. Fine-grained inclusions are a distinct group of refractory inclusions now consisting mostly of secondary alteration products (Grossman and Ganapathy, 1975). Noting that all such objects listed by Clayton et al. (1988) have negative F_{Si} values, we attribute the negative F_{Si} of those objects and the coarse-grained inclu-

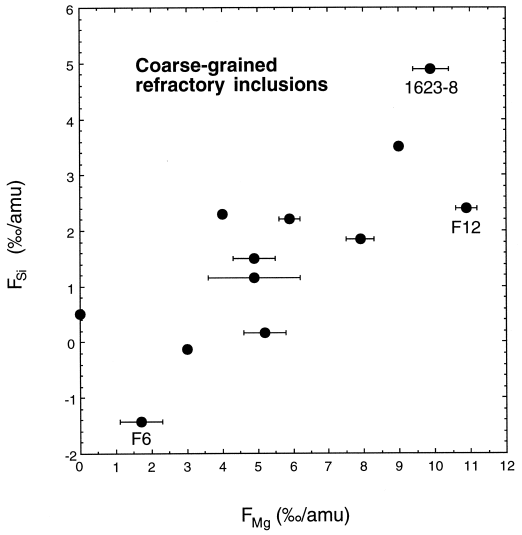

Fig. 6. Silicon and magnesium isotopic mass fractionations in coarse-grained, refractory inclusions.

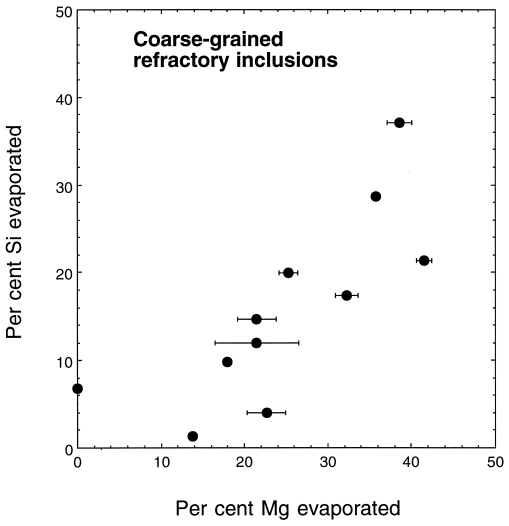

Fig. 7. Amounts of silicon and magnesium evaporated from precursors of coarse-grained, refractory inclusions, calculated from the data in Figure 6, assuming that $SiO_{(g)}$ and $Mg_{(g)}$ are the major evaporating species of each element.

sion, F6, to some effect accompanying secondary alteration, and remove F6 from further consideration in this work.

The Mg and Si isotopic compositions of the remaining coarse-grained inclusions are here assumed to result from kinetic isotope fractionation accompanying evaporation according to the Rayleigh equation. As shown above, $Mg_{(g)}$ and $SiO_{(g)}$ are the dominant evaporating species of Mg and Si, respectively, from a CMAS droplet at 1700 to 2000 K, regardless of whether evaporation occurs in vacuum or in an H_2 gas at any pressure up to 1 bar. This information allows the fractionation factors for Mg and Si to be set at $(24/25)^{0.5}$ and $(44/45)^{0.5}$, respectively, the inverse square roots of the masses of the evaporating species. By using these values, the Mg and adjusted Si isotopic data from Figure 6 were used to calculate the percent of the original Mg and Si evaporated, respectively, from each coarse-grained inclusion, and the resulting data are plotted on Figure 7. The data show that the fraction of the total Si evaporated is, in all cases but one, less than the fraction of the total Mg evaporated from the same inclusion, with most inclusions having undergone 5 to 22% evaporation of Si and 17 to 32% evaporation of Mg. The sample most isotopically fractionated in Si, 1623-8, has an isotopic composition suggesting that 38% of the Si and 39% of the Mg were evaporated, while the sample most isotopically fractionated in Mg, F12, has apparently had 22% of its Si and 42% of its Mg evaporated.

8. EFFECT OF EVAPORATION ON CONDENSATE CHEMICAL COMPOSITIONS

The temperature dependence of $P_{Si}^{tot}/P_{Mg}^{tot}$ and therefore of the relative amounts of Si and Mg evaporated from CMAS liquids was discussed above. To assess the dependence of this ratio on liquid composition, evaporation calculations were done in an H_2-dominated gas at 1700 and 2000 K on each of two potential inclusion precursor compositions: 29.74 wt.% CaO, 10.9% MgO, 37.58% Al_2O_3 and 21.79% SiO_2, a Type A-like composition equal to that of the condensate from a solar gas at 1×10^{-5} bar at 1320 K; and 19.76 wt.% CaO, 18.24% MgO, 24.92% Al_2O_3 and 37.08% SiO_2, a Type B-like composition equal to that of the condensate at 1310 K. The results shown in Figure 8a indicate that the relative amounts of Mg and Si evaporated from CMAS liquids depend heavily on the starting bulk composition. For each composition, the fraction of the Si evaporated for a given fraction of the Mg evaporated is greater at 2000 K than at 1700 K, as seen above. For each temperature, a much greater fraction of the Si is evaporated at a given fraction of the Mg evaporated for the more MgO-, SiO_2-rich, Type B-like composition. Also plotted on Figure 8a are the fractions of the Mg and Si evaporated from the refractory inclusions in Figure 7, as inferred from their isotopic compositions. Comparison with the calculated evaporation curves suggests that the isotopic data for most refractory inclusions, both Type A and Type B, are consistent with evaporation of precursors similar in composition to those selected here at the temperatures illustrated.

In this calculation, as before, $Mg_{(g)}$ and $SiO_{(g)}$ are the dominant evaporating species of Mg and Si, respectively. Both $H_2O_{(g)}$ and $SiO_{(g)}$ contribute significantly to the evaporating oxygen, however, and the relative proportions of the oxygen removed in the form of each molecule vary significantly as the SiO_2 content of the liquid declines with increasing degree of evaporation. To compute the magnitude of oxygen isotopic mass fractionation that would result from evaporation of this much SiO_2 and MgO from inclusion precursors, the Rayleigh fractionation of Mg, Si, and oxygen isotopes was calculated using the inverse square root of the appropriate masses for each molecule at each evaporation step, and the isotopic as well as the chemical composition of the liquids were calculated at each step. In Figure 8b, the resulting F_O is plotted against F_{Mg} for the two temperatures and starting bulk compositions. The degree of mass fractionation of oxygen for a specific degree of mass fractionation of Mg increases with increasing evaporation temperature for both compositions, and is greater for the more SiO_2-rich, Type B-like starting composition at any given tem-

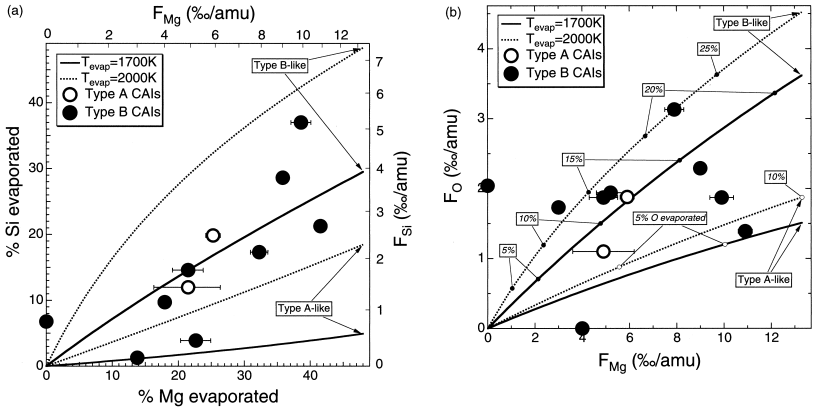

Fig. 8. (a) Calculated amounts of silicon and magnesium evaporated at 1700 and 2000 K from a relatively SiO_2-poor, Type A-like and a relatively SiO_2-rich, Type B-like condensate precursor, compared to amounts inferred from the Mg and Si isotopic compositions of Types A and B inclusions. (b) Calculated magnesium and oxygen isotopic compositions of evaporation residues produced at 1700 and 2000 K from the Type A-like and Type B-like condensate precursors, compared with the isotopic compositions of Types A and B inclusions. Numbers along curves represent calculated percentages of the initial oxygen evaporated.

perature. The latter effect is due to the higher MgO and SiO_2 contents relative to CaO and Al_2O_3 in the Type B-like composition compared to the Type A-like one. A given fraction of the Mg lost from a Type B-like composition results in a greater fraction of the oxygen lost than in a Type A-like composition. The oxygen isotopic compositions for the inclusions whose Si and Mg isotopic data are given in Figure 6 (Clayton et al., 1988) are also plotted on Figure 8b. More inclusions have oxygen isotopic compositions compatible with evaporation of the Type B-like composition than the Type A-like one. The largest Mg isotopic mass fractionations seen in refractory inclusions are 10 to 11‰/amu. The calculations presented here suggest that, for Mg isotopic fractionations this large, the maximum oxygen isotopic mass fractionations expected are 3 to 4‰/amu, corresponding to evaporation of 18 to 26% of the initial oxygen. This compares favorably with the observed spread of oxygen isotopic compositions of refractory inclusions about the carbonaceous chondrite anhydrous mixing line of 3‰/amu, measured in the slope-1/2 direction (Clayton et al., 1988). According to Clayton et al. (1977), refractory inclusions exchanged their oxygen isotopic compositions with a reservoir near the terrestrial line subsequent to high-temperature evaporation and condensation processes. The true magnitude of isotopic fractionation before exchange must be obtained by extrapolation from the reservoir composition through each bulk composition to a mass fractionation line passing through $\delta^{18}O \sim \delta^{17}O \sim -40‰$. Although not done here due to uncertainty in the reservoir composition, this extrapolation could easily double the observed range of oxygen isotopic mass fractionation. The maximum range of oxygen isotopic fractionations predicted from the evaporation calculations would lie comfortably within the extrapolated range.

We now address the question of whether the degree of evaporation of MgO and SiO_2 consistent with isotopic compositions of coarse-grained inclusions is sufficient to bring their bulk chemical compositions into agreement with those of predicted high-temperature condensates. In this discussion, consideration is restricted to the trajectory of bulk compositions calculated for the equilibrium condensate assemblage for a solar gas at 1×10^{-5} bar. Figures 9a–c, plots of SiO_2 vs. MgO, are a close-up view of this trajectory in the temperature range where melilite reacts with the gas to form fassaitic pyroxene, i.e., where the Type A condensate assemblage is converted to the Type B one. Note the large jump in the SiO_2 content of the condensate, from ~23 wt.% to ~37 wt.%, between 1314 K and 1312 K, the interval over which this occurs.

To show how subsequent evaporation could have modified condensate compositions, evaporation calculations were conducted at $P_{H_2} = 1 \times 10^{-8}$ bar at 1700, 1800, 1900, and 2000 K for various starting compositions along the condensate trajectory. Figures 9a–c show some of the calculated evaporation paths emanating from calculated initial compositions along the condensate trajectory, some of which are labelled with their condensation temperatures. As expected, for each starting composition, there is a progressively greater absolute reduction in SiO_2 content for a given reduction in MgO content with increasing evaporation temperature. Also as expected, for a given evaporation temperature, the absolute reduction in SiO_2 content for a given reduction in MgO content decreases progressively with decreasing SiO_2 content of the starting composition. Furthermore, because high-temperature, melilite-bearing condensate assemblages have lower MgO and SiO_2 contents, 5 to 12 and 18 to 22 wt.%, respectively, than lower-temperature, fassaite-bearing ones, 13 to 18 and 23 to 37%, the absolute change in MgO or SiO_2 content for a particular fraction of the Mg or Si evaporated is smaller for the melilite-bearing assemblages. Temperatures of crystallization of spinel and gehlenite from liquids having the compositions of all starting condensates and evaporation residues were computed by using the Berman (1983) model. Spinel was found to be present for all compositions investigated at evaporation temperatures of 1700 and 1800 K, for about half of the compositions at 1900 K and for none of the compositions at 2000 K. Assuming that spinel is inert during evaporation of the melt, calculations were performed to determine the effect of sequestration of solid spinel on the evaporation paths of all starting condensate compositions. Although the amount of spinel present is not known for each composition and temperature, Stolper (1982) found from

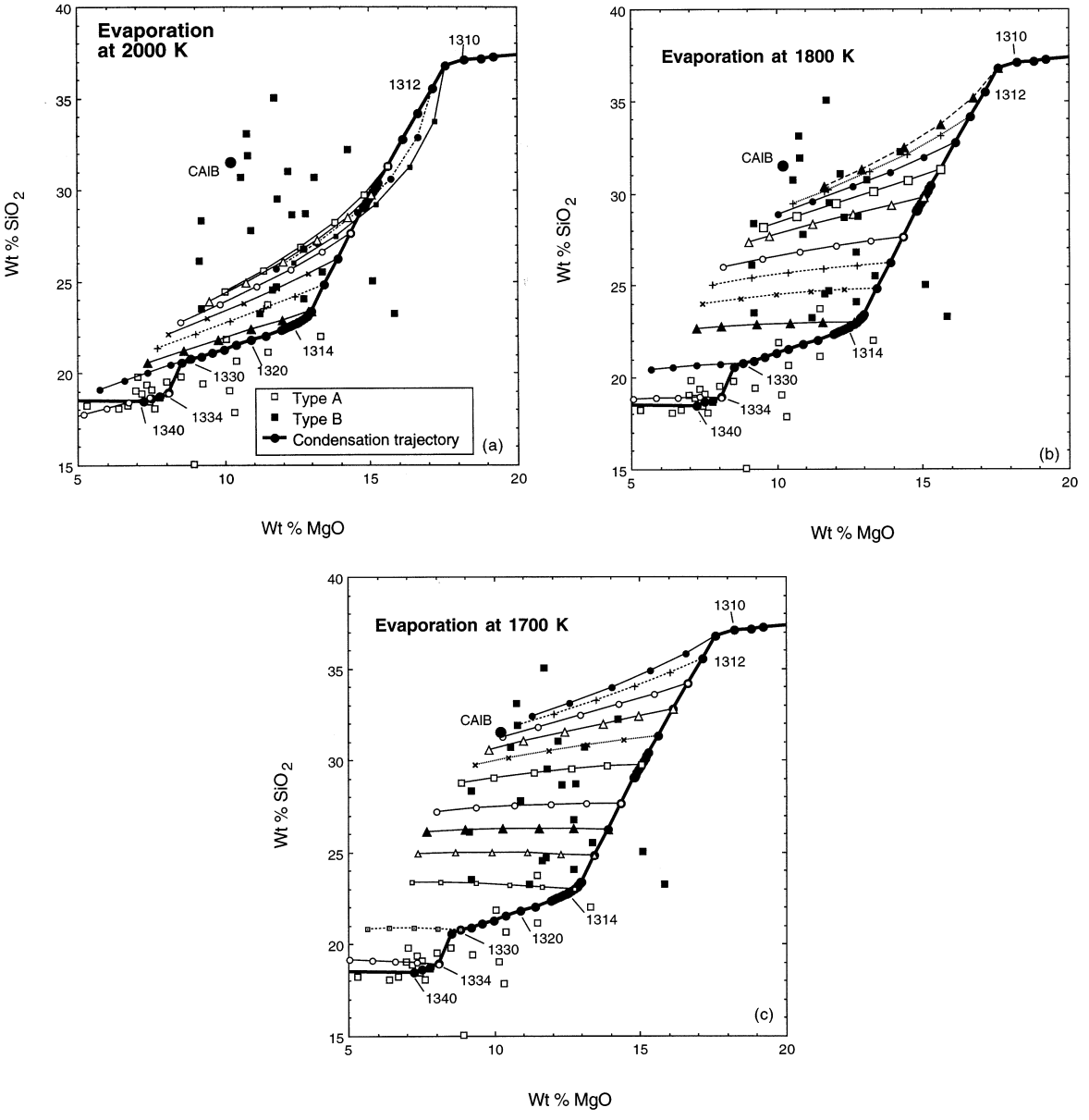

Fig. 9. Comparison between refractory inclusion compositions and those lying along evaporation paths computed at (a) 2000 K; (b) 1800 K; and (c) 1700 K originating from the compositions of equilibrium assemblages of condensates formed in a solar gas at $P^{tot} = 1 \times 10^{-5}$ bar. CAIB is the composition whose liquid–crystal phase relations were studied by Stolper (1982). Compositions along the condensation trajectory are labelled by the temperatures at which they were produced. Evaporation paths emanating from different starting compositions along the condensation trajectory are represented by different symbols. The symbols along the evaporation paths mark compositions produced at increments of 10% of the initial Mg evaporated, from 10% closest to the condensation trajectory to 50% furthest away.

3 to 8 wt.% spinel in all of his experimental run products of CAIB synthesized above 1700 K. The composition of CAIB is also plotted on Figures 9a–c. Accordingly, a second set of evaporation calculations was performed on each starting composition, after its modification by removal of 10 wt.% stoichiometric $MgAl_2O_4$. Bulk compositions of evaporation residues were computed by adding the sequestered spinel and the evaporated liquid compositions back together again. In all cases, the changes in evaporation paths were insignificant.

At a temperature of 2000 K, the evaporation paths in Figure 9a plunge so steeply that, at the correct MgO contents, predicted SiO_2 contents are below those of most Type B inclusions. The slopes of the evaporation paths gradually become lower, however, with progressively lower evaporation temperatures. As a result, at 1700 K (Fig. 9c), the predicted field of evaporation residues overlaps the bulk compositions of almost all Type B inclusions. Two Type B inclusions have bulk compositions on the high-MgO side of the condensation trajectory, and cannot result from evaporation of any condensate composition at any reasonable temperature. Perhaps their compositions are the result of natural scatter about the condensation trajectory and/or experimental error. Also, two Type B inclu-

sions containing 33 to 35% SiO_2 can probably only be reached by evaporation at temperatures below those considered here and only after >50% Mg evaporation.

Data from the 1700 K evaporation paths were used to construct contours of constant percentages of Mg and Si evaporated from initial condensate compositions in Figures 10a,b, respectively. In Figure 10a, it is seen that the distribution of Type B inclusion compositions within the field of evaporation residues suggests that most Type Bs achieved their compositions after losing between 10 and 30% of their initial Mg, very similar to the above estimates of Mg loss based on Mg isotopic compositions of Type Bs. Also, as seen in Figure 10b, the distribution of Type B inclusion compositions relative to the Si contours suggests that almost all Type Bs lost <20% of their Si, with about half of them losing <5% and half losing >5%, similar to the Si losses estimated from Si isotopic data.

Sample 1623-8 is unique in that it is the only sample considered herein for which both chemical and isotopic compositions are available. While both types of data suggest that 1623-8 is among the samples that have undergone the largest evaporation losses of both Mg and Si, and the estimates of the amount of Mg lost are similar from chemical, ~45%, and isotopic, ~38%, data, the amount of Si loss estimated from the chemical composition, ~12%, is substantially less than that indicated by its isotopic composition, ~37%.

Bulk chemical composition data for Type A inclusions scatter much more closely about the condensation trajectory than those for Type Bs, and most are probably within measurement error of the condensation trajectory shown. When plotted on a graph of this kind, however, bulk chemical changes due to evaporation of large fractional amounts of MgO and SiO_2 from starting compositions on this part of the condensation trajectory are relatively small. As a result, bulk chemical compositions of many Type A inclusions are compatible with as much as 30% evaporation of Mg at 1700 K (Fig. 10a) but less than 5% evaporation of Si (Fig. 10b). On Figure 8a, the two Type A inclusions whose isotopic compositions have been measured indeed appear to have lost 20 to 25% of their initial Mg, but compared to this, significantly more of their Si, 10 to 20%, than indicated by Figure 10b. Perhaps some Type A inclusions underwent evaporation at higher temperatures than Type Bs. If, for example, the condensate assemblage at 1332 K were evaporated at 2000 K, a composition within the field of Type As would be produced as a result of 25% evaporation of Mg and 8% evaporation of Si (Fig. 9a).

This discussion has focussed solely on agreement between spinel-corrected compositions of refractory inclusions and those predicted for evaporation residues on a plot of SiO_2 vs. MgO contents. Although inclusion compositions generally lie much closer to the condensation trajectory on the other oxide–oxide plots in Figure 2 than they do in the SiO_2–MgO plot, Figure 2f, the composition contours for evaporation residues also lie much closer to their starting compositions on the condensate trajectory in these plots. Although these plots are not shown, agreement is excellent. Perhaps not so obvious are the positions of the composition contours of evaporation residues on the Stolper projection and in the plane orthogonal to it, and these are illustrated in Figure 11a and b, respectively. Composition contours for residues that formed by 10 to 50% loss of Mg again overlap almost all Types A and B inclusion

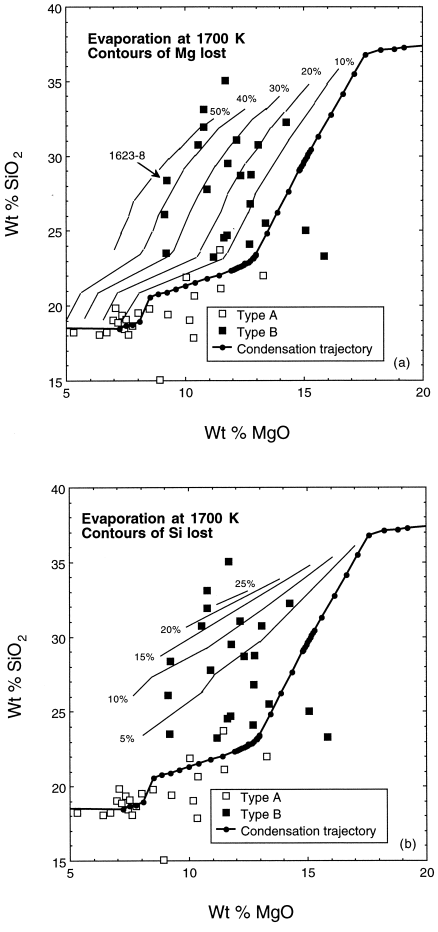

Fig. 10. Comparison between refractory inclusion compositions and those lying along composition contours at constant percentages of the initial (a) Mg and (b) Si evaporated at 1700 K from the compositions of equilibrium assemblages of condensates formed in a solar gas at 1×10^{-5} bar.

compositions in Figure 11a. In Figure 2g, excellent agreement is observed between inclusion compositions and the trajectory of condensates at 1×10^{-5} bar. Because composition contours of evaporation residues lie so close to compositions along that condensation trajectory in Figure 11b, agreement between inclusion compositions and those of evaporation residues is no poorer on this figure.

Almost all Types A and B inclusion compositions have been explained in terms of non-equilibrium evaporation of starting materials whose compositions lie along a trajectory of compositions resulting from equilibrium condensation, or equilibrium evaporation, under a specific set of conditions, i.e., at 1×10^{-5} bar in a gas of solar composition. Although composition trajectories calculated for equilibrium condensation over a wide range of physico-chemical conditions would serve equally well as starting points for production of inclusion compositions by non-equilibrium evaporation, some would not. As seen in Figure 2f, for example, condensation from a solar gas at 1×10^{-1} bar and from a gas enriched in dust by a factor of 20 relative to C1 chondrites at 1×10^{-3} bar produce trajectories of compositions much lower in MgO at 25 to 35 wt.% SiO_2 than the

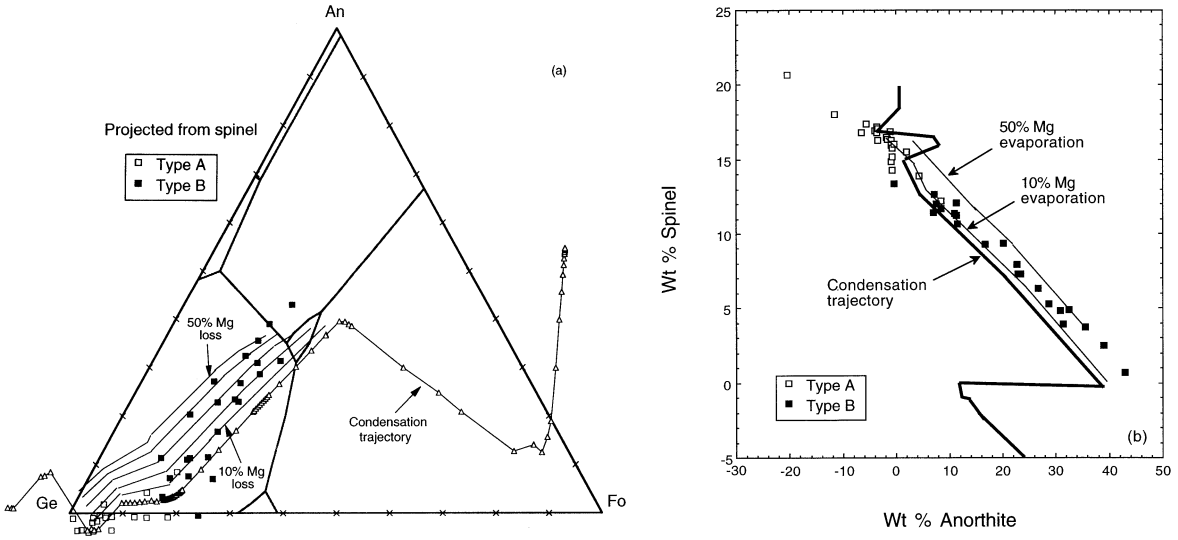

Fig. 11. Composition contours of evaporation residues of starting compositions on the condensation trajectory of a solar gas at 1×10^{-5} bar, compared to inclusion compositions (a) projected from Spinel onto the Gehlenite–Forsterite–Anorthite plane; and (b) orthogonal to that plane.

trajectory used above. It may not be possible to convert these compositions to those of Type B inclusions by evaporation at reasonable temperatures of the amounts of MgO and SiO_2 indicated by isotopic measurements.

9. CONCLUSION

This work suggests that each Type A and B inclusion could have formed by condensation or evaporation with a composition close to that expected of the equilibrium assemblage at a specific temperature and pressure. After most of the remaining Mg and Si were removed from the nebular gas, presumably into lower-temperature condensates, refractory inclusions underwent non-equilibrium evaporation above their melting temperatures, releasing $SiO_{(g)}$ and $Mg_{(g)}$ into a gas that was undersaturated in Si and Mg. The strength of the model presented lies in the agreement between the degree of evaporation inferred from major element oxide compositions and that inferred from Mg and Si isotopic compositions of refractory inclusions; however, the major element data are from one suite of refractory inclusions and the isotopic data from another. The ultimate test of the model awaits measurement of both the bulk chemical compositions of whole inclusions and the magnesium, silicon and oxygen isotopic compositions of the same inclusions.

An important improvement to our computational method for predicting the compositions of evaporation residues will be in generalizing its application to condensed assemblages unrestricted to CMAS and to cosmic gases other than pure H_2.

Acknowledgments—We are grateful for helpful discussions with R. N. Clayton and M. Humayun. N.M.P. thanks A. Hashimoto for mentoring, and allowing him access to his experimental facilities at the University of Hokkaido. This work was supported by the National Aeronautics and Space Administration through Grants NAG5–4476 (LG), NAG5–4298 (AMD) and NAG5–6972 (FMR).

REFERENCES

Beckett J. R. (1986) The origin of calcium-, aluminum-rich inclusions from carbonaceous chondrites: an experimental study. Ph.D. thesis, Univ. Chicago.

Berman R. G. (1983) A thermodynamic model for multicomponent melts, with application to the system CaO–MgO–Al_2O_3–SiO_2. Ph.D. thesis, Univ. Br. Columbia.

Chamberlin L., Beckett J. R., and Stolper E. M. (1992) Experimental determination of oxide activities in synthetic CAI and POI melts. *Lunar Planet. Sci.* **XXIII,** 215–216 (abstr.).

Chou C.-L., Baedecker P. A., and Wasson J. T. (1976) Allende inclusions: Volatile-element distribution and evidence for incomplete volatilization of presolar solids. *Geochim. Cosmochim. Acta* **40,** 85–94.

Clarke R. S. Jr, Jarosewich E., Mason B., Nelen J., Gómez M., and Hyde J. R. (1970) The Allende, Mexico, meteorite shower. *Smithson. Contrib. Earth Sci.* **5**.

Clayton R. N., Onuma N., Grossman L., and Mayeda T. K. (1977) Distribution of the pre-solar component in Allende and other carbonaceous chondrites. *Earth Planet. Sci. Lett.* **34,** 209–224.

Clayton R. N., Mayeda T. K., MacPherson G. J., and Grossman L. (1987) Oxygen and silicon isotopes in inclusions and chondrules from Vigarano. *Lunar Planet. Sci.* **XVIII,** 185–186 (abstr.).

Clayton R. N., Hinton R. W., and Davis A. M. (1988) Isotopic variations in the rock-forming elements in meteorites. *Phil. Trans. R. Soc. Lond.* **A325,** 483–501.

Davis A. M., Hashimoto A., and Richter F. M. (1998) Isotopic mass fractionation under solar nebular conditions. *Meteoritics Planet. Sci.* **33,** A39. (abstr.).

Ebel D. S. and Grossman L. (2000). Condensation in dust-enriched systems. *Geochim. Cosmochim. Acta* **64,** 339–366.

El Goresy A., Nagel K., and Ramdohr P. (1979) Spinel framboids and fremdlinge in Allende inclusions: Possible sequential markers in the early history of the solar system. *Proc. Lunar Planet. Sci. Conf. 10th*, 833–850.

Grossman L. (1972) Condensation in the primitive solar nebula. *Geochim. Cosmochim. Acta* **36,** 597–619.

Grossman L. (1975) Petrography and mineral chemistry of Ca-rich inclusions in the Allende meteorite. *Geochim. Cosmochim. Acta* **39,** 433–454.

Grossman L. and Ganapathy R. (1975) Volatile elements in Allende inclusions. *Proc. Lunar Sci. Conf. 6th*, 1729–1736.

Hashimoto A. (1998) Absolute reaction rates of hydrogen with con-

densed phases in the nebula. *Meteoritics Planet. Sci.* **33,** A65 (abstr.).

Loss R. D., Lugmair G. W., Davis A. M., and MacPherson G. J. (1994) Isotopically distinct reservoirs in the solar nebula: Isotope anomalies in Vigarano meteorite inclusions. *Ap. J.* **436,** L193–L196.

MacPherson G. J. and Davis A. M. (1993) A petrologic and ion microprobe study of a Vigarano Type B refractory inclusion: Evolution by multiple stages of alteration and melting. *Geochim. Cosmochim. Acta* **57,** 231–243.

MacPherson G. J., Wark D. A., and Armstrong J. T. (1988) Primitive material surviving in chondrites: Refractory inclusions. In *Meteorites and the Early Solar System* (eds. J. F. Kerridge and M. S. Matthews), pp. 746–807. Univ. Arizona Press.

Mao X.-Y., Ward B. J., Grossman L., and MacPherson G. J. (1990) Chemical compositions of refractory inclusions from the Vigarano and Leoville carbonaceous chondrites. *Geochim. Cosmochim. Acta* **54,** 2121–2132.

Molini–Velsko C., Mayeda T. K., and Clayton R. N. (1986) Isotopic composition of silicon in meteorites. *Geochim. Cosmochim. Acta* **50,** 2719–2726.

Nazarov M. A., Ulyanov A. A., Korina M. I., and Kolesov G. M. (1982) Efremovka CAI's: Major and trace element chemistry. *Lunar Planet. Sci.* **XIII,** 584–585 (abstr.).

Niederer F. R. and Papanastassiou D. A. (1984) Ca isotopes in refractory inclusions. *Geochim. Cosmochim. Acta* **48,** 1279–1293.

Palme H. and Wlotzka F. (1979) A Ca, Al-rich inclusion from the Leoville (C3V)-meteorite. *Meteoritics* **14,** 508–511 (abstr.).

Simon S. B., Davis A. M., and Grossman L. (1999) Origin of compact type A refractory inclusions from CV3 carbonaceous chondrites. *Geochim. Cosmochim. Acta* **63,** 1233–1248.

Stolper E. M. (1982) Crystallization sequences of Ca–Al-rich inclusions from Allende: An experimental study. *Geochim. Cosmochim. Acta* **46,** 2159–2180.

Sylvester P. J., Grossman L., and MacPherson G. J. (1992) Refractory inclusions with unusual chemical compositions from the Vigarano carbonaceous chondrite. *Geochim. Cosmochim. Acta* **56,** 1343–1363.

Sylvester P. J., Simon S. B., and Grossman L. (1993) Refractory inclusions from the Leoville, Efremovka, and Vigarano C3V chondrites: Major element differences between Types A and B, and extraordinary refractory siderophile element compositions. *Geochim. Cosmochim. Acta* **57,** 3763–3784.

Tsuchiyama A., Tachibana S., and Takahashi T. (1999) Evaporation of forsterite in the primordial solar nebula; rates and accompanied isotopic fractionation. *Geochim. Cosmochim. Acta* **63,** 2451–2466.

Wänke H., Baddenhausen H., Palme H., and Spettel B. (1974) On the chemistry of the Allende inclusions and their origin as high temperature condensates. *Earth Planet. Sci. Lett.* **23,** 1–7.

Wark D. A. (1981) The pre-alteration compositions of Allende Ca–Al-rich condensates. *Lunar Planet. Sci.* **XII,** 1148–1150 (abstr.).

Wark D. A. and Lovering J. F. (1977) Marker events in the early evolution of the solar system: Evidence from rims on Ca–Al-rich inclusions in carbonaceous chondrites. *Proc. Lunar Sci. Conf.* **8,** 95–112.

Wark D. A. and Lovering J. F. (1982) The nature and origin of type B1 and B2 Ca–Al-rich inclusions in the Allende meteorite. *Geochim. Cosmochim. Acta* **46,** 2581–2594.

Yoneda S. and Grossman L. (1995) Condensation of CaO–MgO–Al_2O_3–SiO_2 liquids from cosmic gases. *Geochim. Cosmochim. Acta* **59,** 3413–3444.